Ecotoxicology and Environmental Safety 309 (2026) 119520

Contents lists available at ScienceDirect

Ecotoxicology and Environmental Safety

journal homepage: www.elsevier.com/locate/ecoenv

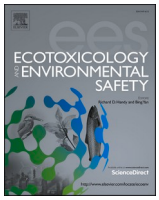

Gut microbiota-derived indole-3-Acetic Acid attenuates skeletal fluorosis via AHR-mediated suppression of Wnt/β-Catenin signaling

Jiantong Wei [a,b,c,d,1], Xingchao Chen [a,b,c,1], Guohua Chen [e], Qingqing Qin [d], Hao Chen [d], Wenqiang Liang [d], Wei Zhang [a,b,c], Shengshan Xue [a,b,c], Wenji Wang [f,*], Yongping Wang [g,*]

[a] Department of Orthopedics, Zhangye People's Hospital Affiliated to Hexi University, Zhangye, Gansu 734000, China
[b] Hexi University Institute Bone and Joint, Zhangye, Gansu 734000, China
[c] Orthopedics Quality Control Center of Zhangye City, Zhangye, Gansu 734000, China
[d] The First Clinical Medical College of Lanzhou University, Lanzhou, Gansu 730000, China
[e] Gansu Provincial Center for Disease Control and Prevention, Lanzhou, Gansu 730000, China
[f] Department of Orthopedics, The First Hospital of Lanzhou University, Lanzhou, Gansu 730000, China
[g] Department of Orthopedics, The Second Affiliated Hospital of Hainan Medical University, Haikou, Hainan 570311, China

ARTICLE INFO

Edited by Tao Zhang

Keywords:
Skeletal fluorosis
Gut microbiota
Indole-3-Acetic Acid
Aryl hydrocarbon receptor
Osteoblast differentiation

ABSTRACT

Chronic fluoride exposure causes skeletal fluorosis (SF), a debilitating bone disease, but the lack of a comprehensive understanding of its pathogenesis has hindered the development of effective therapies. Although fluoride is known to stimulate osteoblasts, the role of gut-bone crosstalk in SF remains uninvestigated. In this study, using a rat SF model and in vitro osteoblast studies, we found that fluoride disrupted gut microbial tryptophan metabolism, resulting in decreased serum levels of indole-3-acetic acid (3-IAA) in both SF model rats and human SF patients. This deficiency in 3-IAA impaired the activation of aryl hydrocarbon receptor (AHR), leading to Wnt/β-Catenin pathway hyperactivation, excessive osteoblast differentiation/mineralization, and pathological bone formation. Restoring 3-IAA levels, either through direct supplementation or an intermittent high-tryptophan diet-reactivated AHR, suppressed Wnt/β-Catenin signaling, and alleviated bone damage in vivo. Crucially, knockdown or inhibition of AHR abolished the protective effect of 3-IAA, confirming that the 3-IAA-AHR axis is essential for mitigating SF. In conclusion, we identify a gut microbiota-3-IAA-AHR-Wnt/β-Catenin axis that drives the pathogenesis of SF, and our findings suggest that intermittent tryptophan supplementation could serve as a novel therapeutic strategy to reduce fluoride-induced bone damage by restoring microbial metabolite signaling.

1. Introduction

Fluoride is a naturally occurring trace element widely present in the environment. Prolonged exposure to fluoride via drinking water, food, or air can cause fluorosis (Wu et al., 2022; Wei et al., 2019). Once ingested, fluoride is absorbed into the bloodstream in its ionized form and distributed throughout the body. Due to the strong affinity of fluoride for mineralized tissues, more than 90 % of absorbed fluoride accumulates in bone (Whitford, 1994; Veneri et al., 2023a; Taher et al., 2024). SF, a debilitating metabolic bone disorder caused by chronic excessive fluoride intake, is a major public health issue affecting millions of people in approximately 25 countries (Sellami et al., 2020; Jiang et al., 2020). Clinical symptoms of SF include joint pain, impaired mobility, and in severe cases, permanent disability, imposing significant economic burdens and psychological distress on affected individuals (Veneri et al., 2023b). However, the exact pathogenesis of SF remains incompletely understood.

Bone homeostasis is maintained through a dynamic balance between osteoblast-mediated bone formation and osteoclast-mediated bone resorption (Yamaguchi, 2012). Fluoride disrupts this balance by enhancing osteoblast activity, thereby contributing to the development of SF. Recent studies suggest that aberrant osteoblast function and dysregulated bone remodeling are central to the pathogenesis of SF (Ding et al., 2023; Qiao et al., 2021). During bone formation, osteoblasts

* Corresponding authors.
E-mail addresses: 249640821@qq.com (W. Wang), wangyongpinglzu@163.com (Y. Wang).
[1] These authors contributed equally to this paper.

https://doi.org/10.1016/j.ecoenv.2025.119520
Received 9 September 2025; Received in revised form 12 November 2025; Accepted 2 December 2025
Available online 10 December 2025

secrete a non-mineralized collagen matrix and facilitate removal of pyrophosphate through alkaline phosphatase (ALP) activity, initiating matrix mineralization (Cotti et al., 2020). In the later stages, osteocalcin (OCN) secreted by osteoblasts promotes calcium deposition and further mineralization of the bone matrix (Tsao et al., 2017). Chronic fluoride exposure has been shown to increase ALP activity, enhance osteoblast function, and promote bone mineralization (Bhawal et al., 2015). Additionally, fluoride can accelerate osteoblast maturation by activating the Wnt/β-Catenin signaling pathway (Chu et al., 2020; Guo et al., 2022). Nevertheless, the precise molecular mechanisms underlying fluoride-induced osteoblast activation have not been fully clarified.

Excessive fluoride intake can damage the structural integrity of the ileum and cecum, impair the intestinal mucosal barrier, and alter the diversity and composition of the gut microbiota in mice (Liu et al., 2019; Fu et al., 2020). Dysbiosis may compromise intestinal barrier function and contribute directly to disease development (Chelakkot et al., 2018). The gut microbiota plays a pivotal role in regulating bone metabolism. Increased levels of Bifidobacterium longum and Lactobacillus reuteri enhance bone density by promoting the absorption of essential minerals such as calcium, phosphorus, and magnesium (Ye et al., 2022). Moreover, Akkermansia muciniphila facilitates bone formation and inhibits bone resorption through the release of extracellular vesicles into bone tissue, a mechanism shown to mitigate bone loss in mouse models of postmenopausal osteoporosis (Liu et al., 2021). Epidemiological studies have reported that children with dental fluorosis living in high-fluoride-exposure areas exhibit slightly reduced microbial diversity and richness compared to healthy controls (Mo et al., 2023). Notably, the relative abundances of the genera Corynebacterium, Lachnospiracea incertae sedis, Roseburia, and Turicibacter show significant negative correlations with fluoride concentrations (Zhong et al., 2022). However, the interplay between fluoride exposure, gut microbiota composition, and osteoblast activation remains unclear.

In this study, we established a rat model of SF and investigated the effects of fluoride exposure through drinking water on microbiota using metagenomic sequencing. Our results demonstrated that chronic fluoride exposure disrupts the composition of the gut microbiota and impairs tryptophan metabolism, thereby interfering with microbial-osteal crosstalk. Specifically, reduced activation of AHR signaling by 3-IAA enhances osteogenesis driven by the Wnt/β-Catenin pathway. Furthermore, we identified an intermittent high-tryptophan diet as a novel therapeutic strategy to alleviate skeletal fluorosis, providing a promising avenue for targeted intervention.

2. Materials and methods

2.1. Establishment of rat fluorosis model

Adult Sprague-Dawley rats were obtained from Shouzheng Pharma Biotechnology Co., Ltd. (Wuhan, China) were housed under standard laboratory conditions (22 ± 3°C, 12-h light/dark cycle) with ad libitum access to standard rodent chow. All animal experiments conducted in this study were reviewed and approved by the Ethics Committee of Zhangye People's Hospital Affiliated to Hexi University with the approval number: HFYER-B-202542. After a 7-day acclimatization period, rats were randomly assigned to two groups: (1) Fluorosis Model Group (n = 6): Received sodium fluoride (NaF) dissolved in distilled water at a concentration of 150 mg/L as their sole drinking source; (2) Control Group (n = 6): Received fluoride-free distilled water. At the end of the 60-day treatment period, femorals were processed as follows: Micro-Computed Tomography (μCT), IHC, HE and qPCR.

2.2. Study participants

Human serum samples were obtained from a total of 12 adult participants, all patients in this study were recruited from Jing'an Township, Ganzhou District, Zhangye City, Gansu Province, a known high-fluoride area. The cohort consisted of 8 males and 4 females, with a mean age of 53 years (range 49–59). Detailed demographic information for the cohort is provided in the Table 1.

2.3. Micro-CT assessment

After a 60-day treatment, bone microarchitecture parameters in distal femorals were examined through a micro-CT scanner (NMC-200, NEMO). We defined the region of interest (ROI) as a 2-mm coronary segment located 0.5 cm beneath the growth plate of the distal femur. The micro-CT analysis evaluated key trabecular parameters, including trabecular bone mineral density (Tb.BMD), bone volume fraction (BV/TV), trabecular thickness (Tb.Th), number (Tb.N), and separation (Tb.Sp). Two-and three-dimensional micro-CT images were reconstructed with a micro-CT analysis system at 10 μm resolution (Avatar).

2.4. ELISA

The concentrations of the bone formation marker N-terminal propeptide of type I procollagen (PINP) and the bone resorption marker C-terminal telopeptide of type I collagen (CTX-1) were quantified using commercially available enzyme-linked immunosorbent assay (ELISA) kits specific for rat samples.

2.5. Liquid chromatography-tandem mass spectrometry

The measurements were performed on a Thermo UltiMate 3000 RS chromatographic system coupled to a Thermo TSQ Quantiva mass spectrometer. The method was rigorously validated, and the key parameters are as follows: Limit of Detection (LOD): 0.3 ng/mL; Limit of Quantification (LOQ): 1.0 ng/mL; Recovery Rate: 95.0 % - 105.0 % across low, medium, and high concentration quality control samples. The method also demonstrated excellent linearity ($R^2 > 0.999$) from 1.0 to 500.0 ng/mL.

2.6. Cell culture

MC3T3-E1 cell line was purchased from Procell Life Science & Technology Co., Ltd., and cells were cultured in DMEM (Procell) supplemented with 10 % fetal bovine serum (FBS) and 1 % penicillin-streptomycin solution (Procell) in a humidified incubator (5 % CO_2, 37°C).

2.7. MTT

MC3T3-E1 cells were seeded into 96 well plates at a density of 2×10^3 cells/well, and treated as follows for 24 h: (1) DMEM (control group); (2) 1 mM NaF; (3) 2 mM 3-IAA; (4) 1 mM NaF + 0.5 mM 3-IAA; (5) 1 mM NaF + 1 mM 3-IAA; (6) 1 mM NaF + 2 mM 3-IAA; CH-223191. All experiments were performed in triplicates. 10 μL of MTT solution (5 mg/mL in PBS or medium) was added to each well. Plates were

Table 1
Demographic Characteristics of the Study Participants.

Group	Gender	Age (years)
Normal	male	57
Normal	female	59
Normal	male	49
Normal	male	48
Normal	male	54
Normal	female	52
Patient	male	55
Patient	male	55
Patient	female	50
Patient	female	51
Patient	male	57
Patient	male	50

incubated for 4 h at 37°C. Subsequently, MTT was carefully aspirated and 100 μL of dimethyl sulfoxide (DMSO) was added to each well, gentle agitation on an orbital shaker for 10 min or until complete dissolution. The absorbance of the dissolved formazan was measured at 490 nm using a microplate reader, with a wavelength of 630–650 nm optionally used for background subtraction.

2.8. Drug treatment

MC3T3-E1 or AHR-knockdown MC3T3-E1 cells were seeded into 6-well plates at a density of 3×10^5 cells/well and allowed to adhere overnight in a complete growth medium. The following day, the medium was replaced with fresh medium containing the AHR antagonist CH-223191 at a final concentration of 20 μM or 3-IAA with a final concentration of 2 mM. Control cells received an equal volume of vehicle only. After 24 h of treatment, the cells were harvested for Western blot analysis. The following shRNA and siRNA sequences were used to target AHR: shAHR target sequences: 5'-GCTCAGGAATTTCCCTACAAA-3'; siAHR target sequences: 5'-TATACCCCAGACCAGCTTCC-3′.

2.9. Calcification and Alizarin Red (AR) staining

To induce calcification, cells were treated with 5 mM sodium phosphate monobasic (NaH_2PO_4) with 1 mM NaF for 7 days. The culture medium containing NaH_2PO_4 and NaF was refreshed every 48 h throughout the 7-day treatment period to ensure consistent reagent concentrations and pH stability. For AR staining, MC3T3-E1 cells were washed twice with PBS, after which cells were fixed in 4 % paraformaldehyde and stained with 1 % AR staining solution (C0140, Beyotime) to visually evaluate mineralized osteoblast levels. Images were taken under optical microscopy (NEXCAM-T20, NOVEL).

2.10. Western blot

Cells were lysed in ice-cold lysis buffer (containing 50 mM Tris, 150 mM NaCl, 0.1 % NP-40, and 1 % Triton X-100) supplemented with 1 mM PMSF, followed by vortexing or sonication. Protein concentration was quantified using the BCA protein assay kit according to the manufacturer's protocol. Equal amounts of protein were separated by SDS-PAGE and subsequently transferred onto PVDF membranes (p0807, Millipore, MA, USA). Membranes were blocked with 5 % non-fat milk in TBST buffer (10 mM Tris-HCl (pH 7.9), 150 mM NaCl, 0.05 % Tween 20) for 2 h at room temperature. Following blocking, membranes were incubated overnight at 4°C with the primary antibodies diluted in TBST (Antibody details are provided in Table 2). After extensive washing with TBST, membranes were incubated with appropriate HRP-conjugated secondary antibodies (1:2000 dilution) for 1 h at room temperature. Protein bands were finally visualized using an enhanced chemiluminescence (ECL) detection system. For quantification, the intensity of the western blot band was analyzed using image J.

Table 2
Antibodies used in WB.

Antibodies	Vendors	Cat.	Host	Working concentration
AHR	Biodragon	BD-PN3489	Rabbit	1:1000
MYH11	ZenBIO	R382378	Rabbit	1:1000
β-actin	Bio-swamp	MAB48206	Mouse	1:2000
Osterix	HUABIO	ER1914–47	Rabbit	1:1000
ALP	Servicebio	GB113300	Rabbit	1:1000
OPN	Servicebio	GB112328	Rabbit	1:1000
RUNX2	Abways	CY5864	Rabbit	1:1000
OCN	HUABIO	ER1919–20	Rabbit	1:1000
COL1A1	HUABIO	HA722517	Rabbit	1:1000
Wnt3a	Biodragon	RM3189	Rabbit	1:1000
β-Catenin	HUABIO	ET1601–5	Rabbit	1:2000

2.11. Quantitative real-time polymerase chain reaction (qPCR)

Total cellular RNA was extracted and reverse-transcribed into cDNA using the reverse transcription kit (K1609, Thermo Scientific, Waltham, USA) following the manufacturer's instructions. qPCR was performed using the ChamQ Universal SYBR qPCR Master Mix (Q711–02, Vazymes, Nanjing, China) with a two-step PCR protocol. The specific primers are provided in Table 3.

2.12. Immunohistochemistry (IHC)

Samples were fixed in 4 % paraformaldehyde (PFA), dehydrated through a graded ethanol series, cleared in xylene, embedded in paraffin, and sectioned at 5 μm thickness. Sections were dewaxed in xylene (2 times, 10 min each) and rehydrated through a descending graded ethanol series to distilled water. Antigen retrieval was performed by heating sections in preheated pH 9.0 EDTA buffer (95–100°C) for 15 min using a water bath or pressure cooker, followed by cooling to room temperature (RT) for 20–30 min. Endogenous peroxidase activity was blocked by incubation with 3 % hydrogen peroxide (H_2O_2) in methanol or PBS for 10 min at RT. Non-specific binding sites were blocked with 5 % bovine serum albumin (BSA) in PBS for 30 min at RT. Sections were then incubated with anti-RUNX2 (1:50, ab192256, Abcam), anti-OCN (1:150, ab93876, Abcam) overnight at 4°C. After washing with PBS, sections were incubated with an HRP-conjugated secondary antibody (1:200, ab6721, Abcam) for 1 h at room temperature. Following PBS washes, immunoreactivity was visualized by incubating with 3,3′-diaminobenzidine (DAB) substrate solution for 5 min, with development monitored microscopically until brown staining developed. Sections were then counterstained with hematoxylin for 1 min, rinsed in tap water, dehydrated through an ascending graded ethanol series, cleared in xylene, and mounted with a synthetic resinous mounting medium. Stained sections were evaluated by light microscopy. For statistical analysis, three sections were selected for each quantitative histological measurement and the average value of parallel samples calculated.

2.13. Hematoxylin and Eosin (HE) staining

Samples were fixed in 4 % PFA, dehydrated through a graded ethanol series, cleared in xylene, embedded in paraffin, and sectioned at 5 μm thickness. Sections were baked at 60°C for 2 h to enhance adhesion. Dewaxing was performed in xylene (2 times, 10 min each), followed by rehydration through a descending graded ethanol series to distilled water. For staining, sections were immersed in hematoxylin solution for 5 min, rinsed in running tap water until clear, differentiated in 1 % acid alcohol (1 % HCl in 70 % ethanol) for a few seconds, rinsed again, and then blued in 0.1 % ammonia water or Scott's tap water substitute until sections turned blue. After rinsing in distilled water, sections were

Table 3
Primer sequences used for quantitative real-time PCR.

Gene	Sequence (5'–3')
Rat-GAPDH-F	CGCTAACATCAAATGGGGTG
Rat-GAPDH-R	TTGCTGACAATCTTGAGGGAG
Rat-ALP-F	GACAGGGCAGAAACTCGCTT
Rat-ALP-R	GACGGAAGAAGGGGTGCTAC
Rat-OCN-F	ACTGCATTCTGCCTCTCTGAC
Rat-OCN-R	TAGCGCCGGAGTCTATTCAC
Rat-RANKL-F	CCATCAATGCTGCCAACATCC
Rat-RANKL-R	GCTGAAGATAGTCCGCAGGTA
Rat-OPG-F	CAACCGAGTGTGCGAATGTG
Rat-OPG-R	TTGCAAACCGTGTTTCGCTC
Rat-Runx2-F	CCATGCCATTTCTGCAACCT
Rat-Runx2-R	CACTCCTTCGGTAGGCACTTG
Rat-Osterix-F	GTCCTGGCAACACTCCTACC
Rat-Osterix-R	GGGCAAAGTCAGACGGGTAA

counterstained in eosin solution for 3 min. Sections were then dehydrated through an ascending graded ethanol series, cleared in xylene (2 times, 5 min each), and mounted with a permanent mounting medium. Stained sections were examined and imaged using a light microscope.

2.14. High-tryptophan diet

For High-tryptophan diet, the SD rats were randomly divided into a control group and a high-tryptophan group. The high-tryptophan group was fed a custom diet containing 1.2 % (w/w) L-tryptophan on alternating days, interspersed with the standard control diet. The control group received the standard diet daily. All animals had ad libitum access to food and water throughout the study period.

2.15. Statistical analysis

The statistical analyses were conducted using Graphpad Prism 10.1 software. The significance level among two groups was calculated using two-tailed unpaired *t*-test. Statistical significance of more than two groups was assessed by the analysis of variance (ANOVA), followed by a Tukey post hoc test. p-value < 0.05 was considered to show a significant difference.

3. Results

3.1. Chronic fluoride exposure enhances osteogenic differentiation in a rat model of SF

Establishing a reliable animal model of skeletal fluorosis is essential for elucidating its pathogenesis. In this study, we developed a rat model of chronic fluoride exposure to investigate the effects of fluoride on bone phenotype and related molecular markers with experimental design illustrated in Fig. 1A. Sprague-Dawley (SD) rats were randomly assigned to a control (Ctrl) group or a fluoride-treated (NaF) group. The Ctrl group had free access to distilled water, while the NaF group received drinking water supplemented with 150 mg/L NaF for 60 days. Body weight was monitored regularly throughout the intervention. At the end of the treatment period, rats were euthanized, and samples were

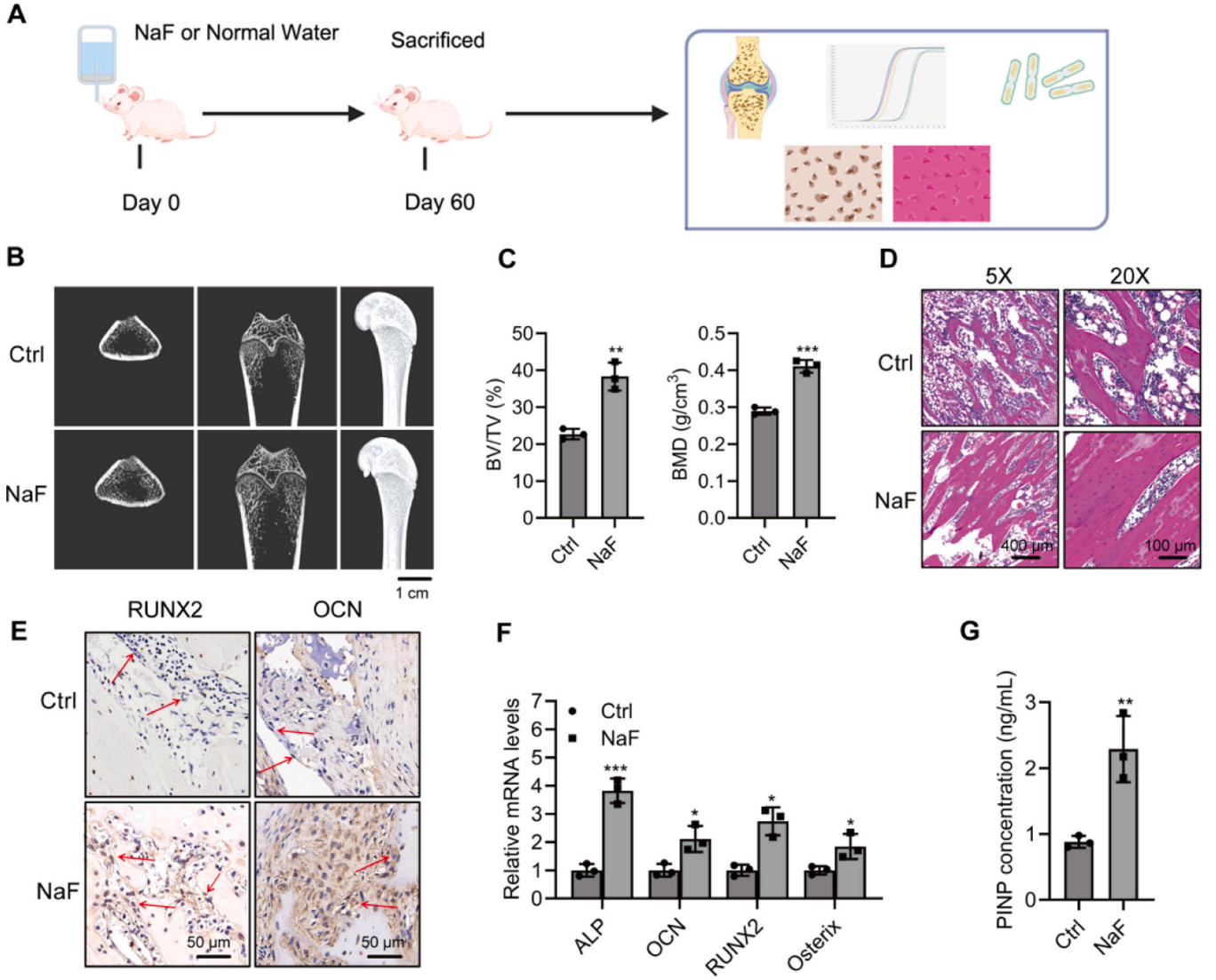

Fig. 1. Fluoride treatment protomes osteogenesis. (A) Experimental schedule for establishing fluorosis rat model. (B) Radiographs of femorals from control (Ctrl) (n = 3) and NaF-treated (n = 3) rats, demonstrating differences in bone density and structure. (C) Bonevolume fration (BV/TV) and Bone mineral density (BMD) measurements from rats in (B). (D) HE-stained pathologic section of rats femoral. (E) Immunohistochemical staining for RUNX2 and OCN in femoral sections, the arrow indicates osteoblasts. (F) Relative mRNA levels of bone-related genes (ALP, OCN, Runx2, and Osterix) in femorals of control (n = 3) and NaF-treated (n = 3) rats, normalized to GAPDH. (G) Serum levels of PINP in control (n = 3) and NaF-treated (n = 3) rats, measured by ELISA. Data are presented as mean ± SD. $^{*}p < 0.05$, $^{**}p < 0.01$, $^{***}p < 0.001$.

collected for bone mineral density assessment, histological analysis of bone tissue, and molecular biology detection. Notably, the teeth of rats in the Ctrl group appeared yellow-brown, whereas the NaF group showed a fading of this coloration (Figure S1A). Micro-computed tomography (micro-CT) of the tibia revealed that compared with the Ctrl group, the NaF group exhibited significant trabecular structural densification, characterized by increased trabecular thickness and enhanced network connectivity (Fig. 1B). Quantitative analysis revealed that both bone volume fraction (BV/TV) and bone mineral density (BMD) were significantly elevated in the NaF group (Fig. 1C), indicating that chronic fluoride exposure stimulates a bone remodeling process dominated by osteogenesis.

HE staining further showed that the NaF group had thickened periosteum, accompanied by proliferating and differentiating osteoblasts, as well as disorganized lamellar bone architecture (Fig. 1D). Quantitative analysis confirmed a significantly larger trabecular bone area in the NaF group compared to the Ctrl group (Figure S1B). Immunohistochemistry results revealed increased expression of RUNX2 (a key transcription factor for osteoblast differentiation) and osteocalcin (OCN, a marker of bone matrix maturation) in the NaF group (Figure 1E, S1C), suggesting enhanced osteoblast activity and matrix synthesis. At the transcriptional level, fluoride exposure significantly upregulated the mRNA expression of osteoblast-related genes, including ALP, OCN, RUNX2, and Osterix (Fig. 1F). In contrast, the expression of RANKL and OPG (a key regulator of osteoclast differentiation) remained unchanged (Figure S1D), implying that fluoride promotes bone formation by

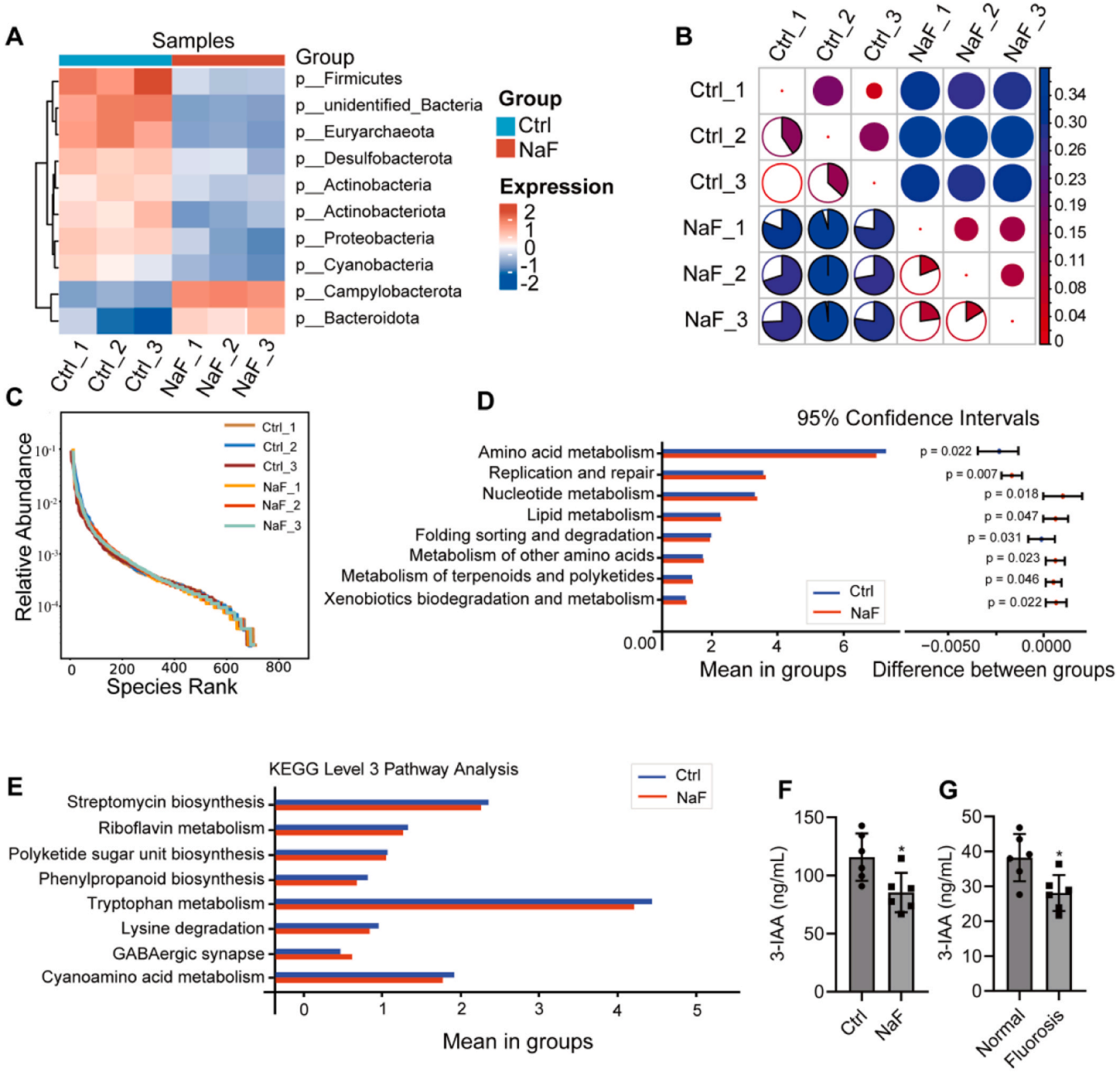

Fig. 2. Fluoride exposure affects the gut microbial profile in patients. (A) Composition of gut microbiota at the phylum level. (B) β-diversity analysis of the microbial community structure. (C) α-diversity analysis of the microbial community structure. (D-E) Functional prediction of gut microbiota based on the KEGG database from 16S rRNA sequencing, showing level 2 (D) and level 3 (E) KEGG pathway results. (F-G) Serum 3-IAA levels detected by mass spectrometry in rats (n = 6) (F) and patients (n = 6) (G) with fluorosis. Data are presented as mean ± SD. *$p < 0.05$.

disrupting the coupling balance between osteoblasts and osteoclasts. Consistently, ELISA results showed a significant increase in serum levels of PINP (a bone formation marker), while the levels of CTX (a bone resorption marker) remained unaltered (Fig. 1 G, S1E).

Taken together, these findings indicate that chronic fluoride exposure for 60 days enhances bone mass primarily by promoting osteoblast differentiation and increasing bone formation.

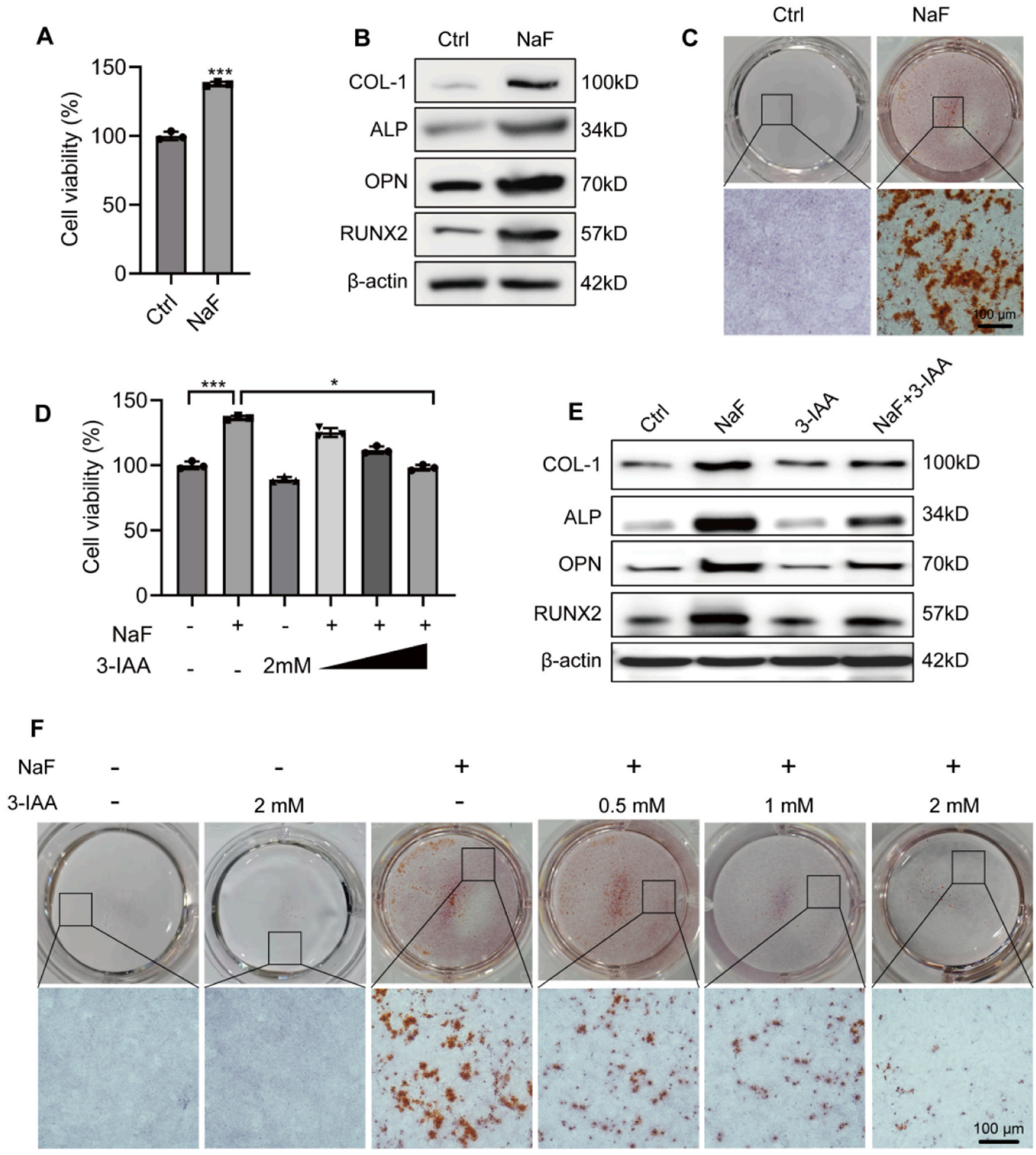

Fig. 3. 3-IAA inhibits NaF-Induced osteoblast differentiation. (A) MTT assay showing cell viability of MC3T3-E1 cells treated with NaF. (B) Western blot analysis of osteogenic markers (COL-1, ALP, OPN, RUNX2) in MC3T3-E1 cells treated with NaF. (C) Alizarin Red staining showing mineralized nodule formation in osteoblasts treated with NaF. (D) MTT assay showing cell viability of osteoblasts treated with NaF in the presence or absence of 3-IAA. (E) Western blot analysis of osteogenic markers (COL-1, ALP, OPN, RUNX2) in MC3T3-E1 cells treated with NaF and/or 3-IAA. (F) Alizarin Red staining showing mineralized nodule formation in MC3T3-E1 cells treated with NaF and/or 3-IAA at different concentrations. Data are presented as mean ± SD. $*p < 0.05$, $***p < 0.001$.

3.2. Chronic fluoride exposure impairs tryptophan metabolism in the gut microbiota and reduces 3-IAA levels

The gut microbiota and its metabolites play a critical role in regulating bone metabolism. To explore their involvement in SF, 16S rRNA gene sequencing combined with KEGG pathway enrichment analysis was performed to examine the effects of chronic fluoride exposure on the composition and functional potential of the intestinal microbiota in rats. At the phylum level, compared with the Ctrl group, the NaF group showed decreased relative abundance of dominant phyla such as Firmicutes and Euryarchaeota, while the relative abundance of Bacteroidetes and Campylobacterota slightly increased (Fig. 2A). Principal coordinate analysis (PCoA) of beta diversity revealed a clear separation between the microbial communities of the Ctrl and NaF groups (Fig. 2B), indicating that chronic fluoride exposure significantly alters the overall structure of the gut microbiota. In contrast, species accumulation analysis revealed no significant difference in alpha diversity between the two groups (Fig. 2C), suggesting that fluoride exposure does not markedly affect microbial evenness.

KEGG pathway analysis demonstrated that eight metabolic pathways, including amino acid metabolism, replication and repair, nucleotide metabolism, and lipid metabolism, were significantly altered in the NaF group compared to the Ctrl group. Among these, disturbances in amino acid metabolism were the most prominent (Fig. 2D), suggesting that chronic fluoride exposure may inhibit amino acid synthesis and catabolism in the gut microbiota. Further analysis of specific pathways showed that tryptophan metabolism, streptomycin biosynthesis, riboflavin metabolism, and phenylpropanoid biosynthesis were downregulated in the NaF group, with tryptophan metabolism exhibiting the most significant change. In contrast, the GABAergic synapse pathway was upregulated (Fig. 2E).

To validate the involvement of microbial tryptophan metabolites, serum levels of 3-IAA (a key tryptophan-derived microbial metabolite) were measured. Rats in the NaF group had significantly lower serum 3-IAA levels than those in the Ctrl group (Fig. 2F). Similarly, serum 3-IAA concentrations were markedly lower in human patients with fluorosis than in healthy individuals (Fig. 2G). These findings suggest that fluoride-induced suppression of microbial tryptophan metabolism reduces systemic 3-IAA levels, which may contribute to the pathogenesis of skeletal fluorosis.

In order to identify which microbial species are the primary producers of 3-IAA, we performed additional analysis by comparing our dataset with established literature on bacterial 3-IAA production (Russell et al., 2013). We identified four relevant genera. The LDA results showed that two of these four genera (*s_Parabacteroides_distasonis* and *s_Bacteroides_eggerthii*) were significantly enriched in the control group, indicating a marked reduction in NaF-treated rats. In contrast, the other two species showed no significant difference in their LDA scores between the two groups (Figure S2).

3.3. 3-IAA mitigates fluoride-induced osteoblast overactivation in vitro

To investigate whether the microbial tryptophan metabolite 3-IAA counteracts fluoride-induced osteoblast overactivation, the effects of NaF on the proliferation, differentiation, and mineralization of MC3T3-E1 osteoblasts were assessed in vitro. Cell viability was measured using the MTT assay after 12 h of exposure to 1 mM NaF. The results showed that NaF significantly enhanced the viability of MC3T3-E1 cells (Fig. 3A). Western blot analysis revealed that NaF treatment markedly upregulated the expression of key osteogenic markers, including type I collagen (COL1), ALP, OPN, and RUNX2, indicating enhanced osteogenic differentiation (figure 3B, S3A). Alizarin Red S staining for matrix mineralization showed that NaF-treated cells formed significantly more mineralized nodules than the control cells (Fig. 3 C, S3B), confirming increased mineralization capacity. Collectively, these findings indicate that NaF promotes osteoblast overactivation by stimulating both early osteogenic differentiation and matrix mineralization, recapitulating the hallmark features of osteoblast dysfunction observed in SF.

Subsequently, the protective effect of 3-IAA against fluoride-induced osteoblast overactivation was validated. MTT assays revealed that pretreatment with 2 mM 3-IAA alone did not alter MC3T3-E1 cell viability. However, co-treatment with 3-IAA and NaF significantly attenuated the NaF-induced increase in cell viability in a dose-dependent manner (Fig. 3D). Western blot analysis demonstrated that 3-IAA co-treatment markedly downregulated the NaF-induced upregulation of osteogenic differentiation markers, including COL1, ALP, OPN, and RUNX2 (figure 3E, S3C-F), indicating that 3-IAA reverses fluoride-induced osteogenic differentiation. Alizarin Red S staining showed that 3-IAA pretreatment alone had no significant effect on mineralized nodule formation, whereas co-treatment with 3-IAA and NaF significantly suppressed NaF-induced mineralization in a dose dependent manner (Fig. 3 F, S3G). Together, these findings suggest that 3-IAA effectively mitigates fluoride-induced osteoblast overactivation by suppressing the abnormal increases in cell viability, reversing the upregulation of osteogenic markers, and inhibiting matrix mineralization.

3.4. 3-IAA pretreatment prevents fluoride-induced osteoblast overactivation in rats

To investigate the protective effects of 3-IAA against SF in vivo, 3-IAA was administered to rats during chronic fluoride exposure. As illustrated in Fig. 4A, SD rats were randomly assigned to a NaF group or a NaF+ 3-IAA treatment group. The NaF group received drinking water containing 150 mg/L NaF for 60 consecutive days. In the NaF+ 3-IAA group, rats were administered 3-IAA (250 mg/kg, oral gavage) from day 40 to day 60. At the end of the intervention, animals were sacrificed for histomorphological and molecular analyses of bone tissue. HE staining revealed that compared with the NaF group, 3-IAA treatment markedly ameliorated periosteal thickening and disorganized lamellar bone architecture induced by NaF (Fig. 4B). Quantitative analysis further demonstrated a significant reduction in trabecular bone area in the 3-IAA group compared to the NaF group (Figure S4A), indicating that 3-IAA mitigated fluoride-induced pathological alterations in bone tissue. Immunohistochemical staining showed that the expression levels of osteogenic markers RUNX2 and osteocalcin (OCN) were significantly reduced following 3-IAA treatment compared to NaF exposure alone (Fig. 4C, S4B), suggesting that 3-IAA suppresses fluoride-induced osteoblast differentiation in vivo.

After 3-IAA treatment, the expression levels of osteoblast-associated genes, ALP, OCN, RUNX2, and Osterix, were significantly downregulated compared to those in the NaF group (Fig. 4D). In contrast, the expression of osteoclast-related genes RANKL and OPG remained unchanged (Figure S4C). Serum ELISA results revealed that 3-IAA significantly reduced the level of PINP, a marker of osteoblast activity, compared to NaF treatment alone (Fig. 4E), while the level of CTX, a marker of bone resorption, was not significantly altered (Figure S4D). Western blot analysis of key proteins in the Wnt/β-Catenin signaling pathway showed that Wnt3a and β-Catenin protein levels were significantly elevated in the NaF group relative to controls, and this upregulation was reversed by 3-IAA treatment (Fig. 4 F, S4E-F). These findings suggest that 3-IAA potentially suppresses osteoblast differentiation and bone formation by inhibiting the activation of the Wnt/β-Catenin pathway.

3.5. 3-IAA inhibits Wnt/β-Catenin signaling via AHR activation

AHR, a known receptor for 3-IAA, can suppress the Wnt/β-Catenin signaling pathway upon ligand activation. To investigate the role of AHR in mediating 3-IAA's regulatory effects on Wnt/β-Catenin signaling, both pharmacological and genetic approaches were employed. First, MC3T3-E1 cells were treated with CH-223191, a selective AHR antagonist (Jing et al., 2025; Han et al., 2024; Cao et al., 2024). We found

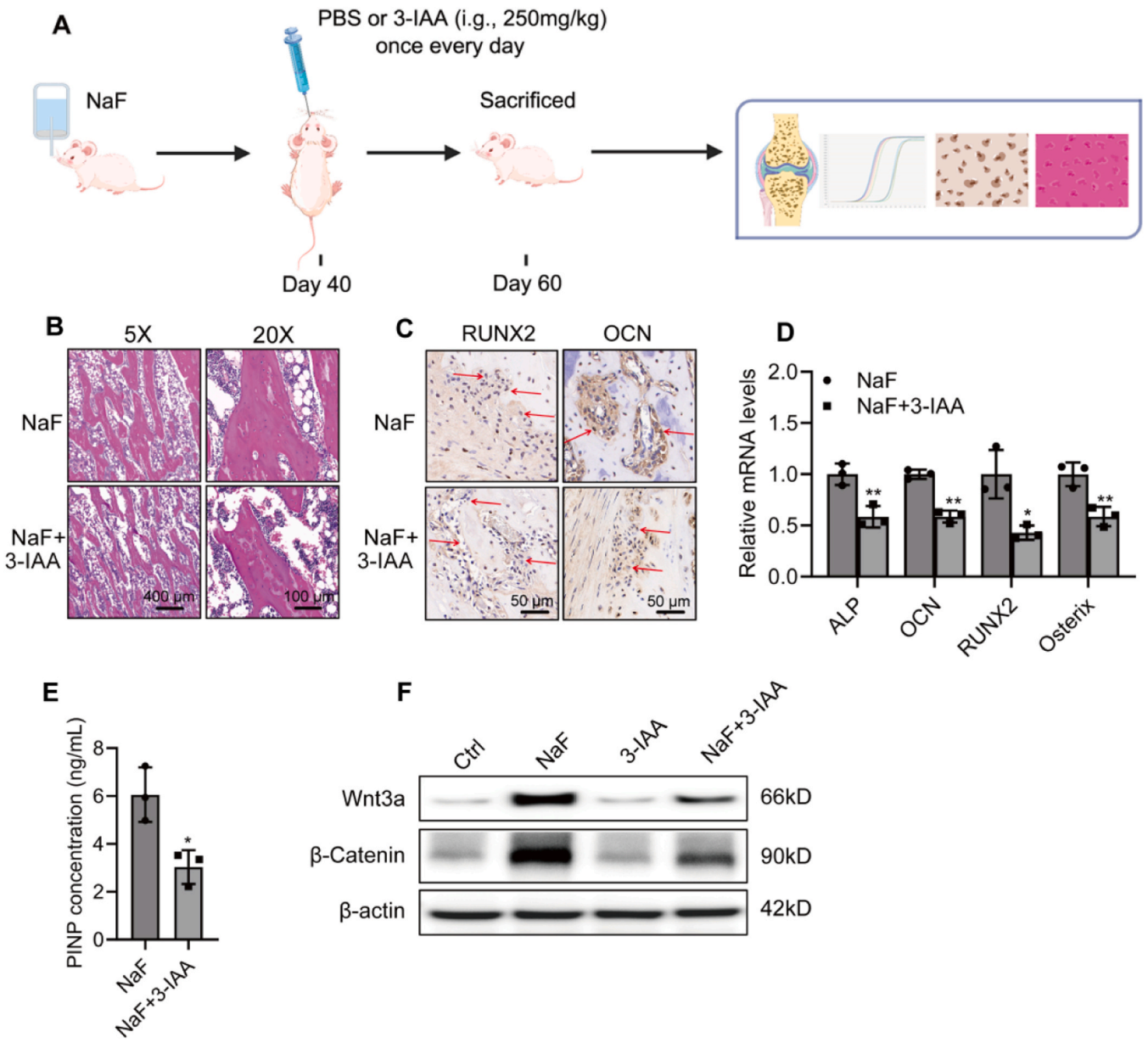

Fig. 4. 3-IAA attenuates NaF-induced osteogenesis via Wnt/β-Catenin signaling. (A) Experimental schedule of experiment. (B) HE-stained sections of rat femoral bone from groups treated with NaF with or without 3-IAA (i.g., 250 mg/kg). (C) Immunohistochemical staining for RUNX2 and OCN in femoral sections, the arrow indicates osteoblasts. (D) Relative mRNA levels of bone-related genes (ALP, OCN, Runx2, and Osterix) in femorals were analyzed from NaF-treated rats either with (n = 3) or without (n = 3) 3-IAA co-administration, normalized to GAPDH. (E) Serum levels of PINP in rats in (A). (F) Western blot analysis of Wnt/β-Catenin signaling pathway proteins (Wnt3a, β-Catenin) in MC3T3-E1 cells of control, NaF-treated, 3-IAA-treated, and NaF+ 3-IAA-treated rats. Data are presented as mean ± SD. $^{*}p < 0.05$, $^{**}p < 0.01$.

CH-223191 abolished the 3-IAA-induced downregulation of Wnt3a and β-Catenin protein levels (Fig. 5A-5B). Similarly, genetic silencing of AHR using shRNA recapitulated this effect, reversing the suppressive action of 3-IAA on Wnt/β-Catenin signaling (Fig. 5C-5D). These findings confirm that AHR mediates the inhibitory effect of 3-IAA on the Wnt/β-Catenin pathway. Next, the functional consequences of AHR knockdown on osteoblast activation were assessed. Silencing AHR in MC3T3-E1 cells significantly reduced AHR protein expression and increased the protein levels of osteogenic markers COL1, ALP, OPN, and RUNX2 (Fig. 5E-5F, Figure S5A-B). To further substantiate the role of AHR in mediating the effects of 3-IAA, we examined the impact of the AHR agonist FICZ. Consistent with our hypothesis, treatment with FICZ alone mimicked the effect of 3-IAA, leading to a significant down-regulation of Wnt3a and β-catenin protein levels and abolished the activity effects of NaF (Figure S5C-F). Taken together, these results demonstrate that AHR is a critical mediator of 3-IAA's suppression of osteoblast differentiation via the Wnt/β-Catenin pathway. Knockdown of AHR abrogates the inhibitory effects of 3-IAA on both Wnt/β-Catenin signaling and osteogenic marker expression.

3.6. Intermittent high-tryptophan diet ameliorates fluoride-induced bone damage via suppression of osteoblast differentiation

Given the effects of the 3-IAA in the fluorosis model, the potential of an intermittent high-tryptophan diet to alleviate SF was further evaluated. As illustrated in Fig. 6A, rats chronically exposed to fluoride for 60 days were randomly assigned to either a high-tryptophan or low-tryptophan group. From day 40 to day 60, the high-tryptophan group

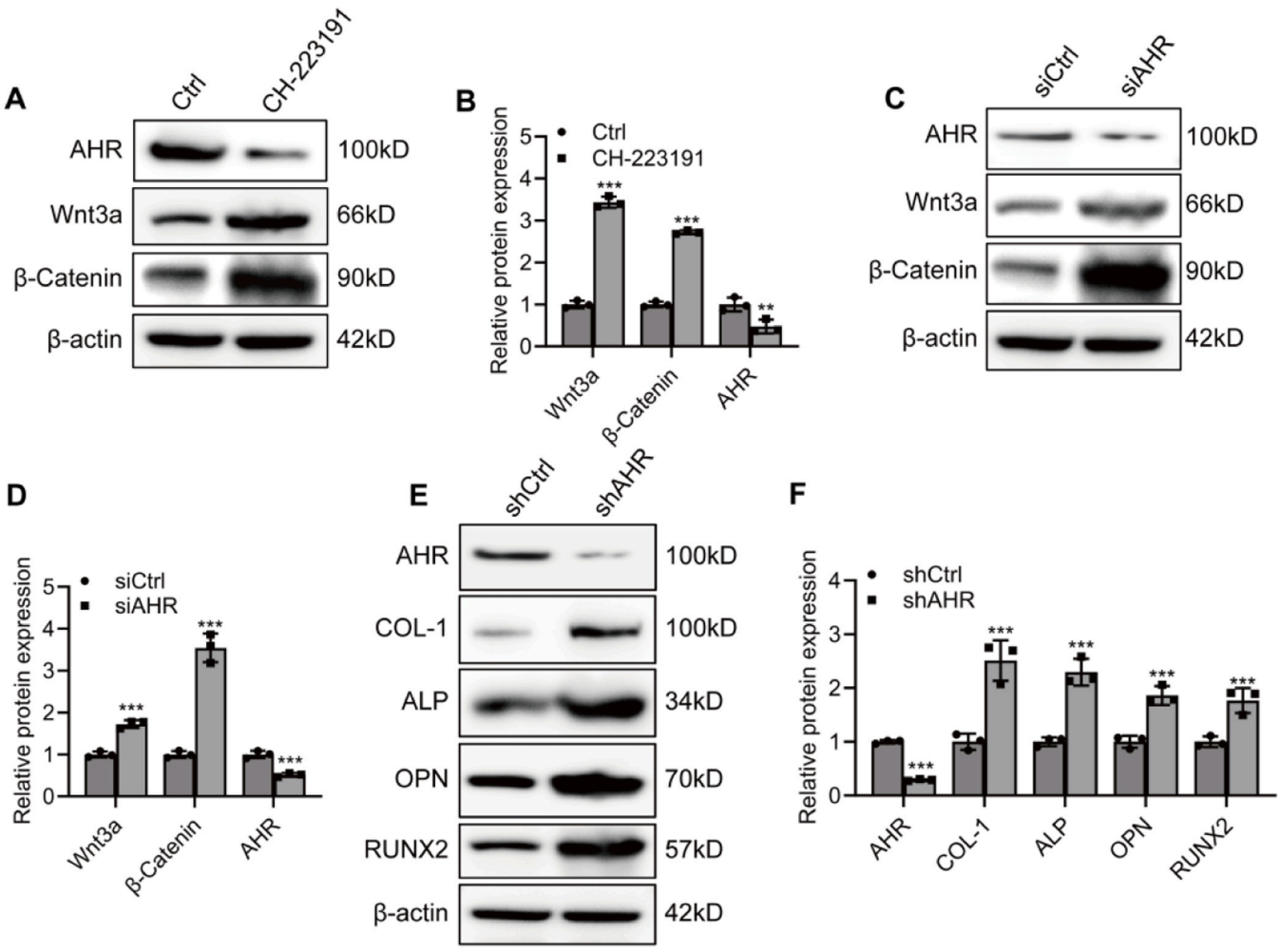

Fig. 5. Activation of AHR is required for 3-IAA to inhibit Wnt/β-catenin signaling and osteogenesis. (A) MC3T3-E1 cells were treated with NaF and 3-IAA in the presence or absence of the AHR inhibitor CH-223191 (20 μM) for 24 h. Western blot analysis of AHR, Wnt3a and β-Catenin protein expression. (B) Quantification of Wnt3a and β-Catenin protein expression in (A). (C) MC3T3-E1 cells were transfected with AHR siRNA or control siRNA and then treated with NaF and 3-IAA. Western blot analysis of AHR, Wnt3a and β-Catenin protein expression. (D) Quantification of AHR, Wnt3a and β-Catenin protein expression in (C). (E) MC3T3-E1 cells transfected with AHR shRNA or control shRNA were treated with NaF and 3-IAA. Western blot analysis of AHR, COL-1, ALP, OPN and RUNX2 protein expression. (F) Quantification of AHR, COL-1, ALP, OPN and RUNX2 protein expression in (E). Data are presented as mean ± SD. $^{**}p < 0.01$, $^{***}p < 0.001$.

received oral gavage of tryptophan at 12 g/kg every other day. At the end of the intervention, the animals were euthanized and samples were collected for BMD assessment, histological analysis, and molecular profiling. Micro-CT imaging revealed that the tibial trabecular architecture in the high-tryptophan group was markedly improved compared to that in the low-tryptophan group (Fig. 6B). Quantitative analysis showed that BMD and BV/TV were significantly higher in the high-tryptophan group (Fig. 6C), indicating that intermittent high-tryptophan intake enhances both bone density and microstructure in fluoride-exposed rats. HE staining further demonstrated that periosteal thickening and lamellar bone disorganization induced by fluoride were significantly attenuated in the high-tryptophan group (Fig. 6D), and the proportion of trabecular bone area was significantly reduced (Figure S6A).

Immunohistochemical staining showed that RUNX2 and OCN were markedly downregulated in the high-tryptophan group (figure 6E, S6B). Consistently, qPCR analysis confirmed that high tryptophan intake significantly reduced mRNA expression of osteoblast-related genes, including ALP, OCN, RUNX2, and Osterix, without significantly affecting the expression of osteoclast-related genes RANKL and OPG (Fig. 6 F, S6C). Serum ELISA further demonstrated that the level of PINP was significantly decreased in the high-tryptophan group, while the level of CTX remained unchanged (Fig. 6 G, S6D). Collectively, these findings indicate that an intermittent high-tryptophan diet effectively mitigates fluoride-induced increases in bone mass and microstructural abnormalities by suppressing osteogenic gene expression and osteoblast activity.

4. Discussion

Over the past half-century, SF has been primarily regarded as a localized bone metabolic disorder in which fluoride directly stimulates bone cells (Kassem et al., 1994; Khokher and Dandona, 1990). Here, we redefine the pathogenesis of SF by identifying a previously unrecognized gut microbiota-metabolite-osteoblast axis as a central driver of disease progression. Through the integration of an SF rat model with multi-omics analyses, we demonstrate that fluoride exposure reduces the production of the microbial metabolite 3-IAA, thereby attenuating AHR signaling in osteoblasts. This loss of AHR activation leads to the hyperactivation of Wnt/β-Catenin signaling, which in turn accelerates osteogenic differentiation and mineralization, thereby exacerbating SF pathology. Collectively, our work shifts the view of fluoride toxicity from a direct skeletal effector to a disruptor of microbial-osteal crosstalk, revealing a critical mechanism in skeletal fluorosis pathogenesis.

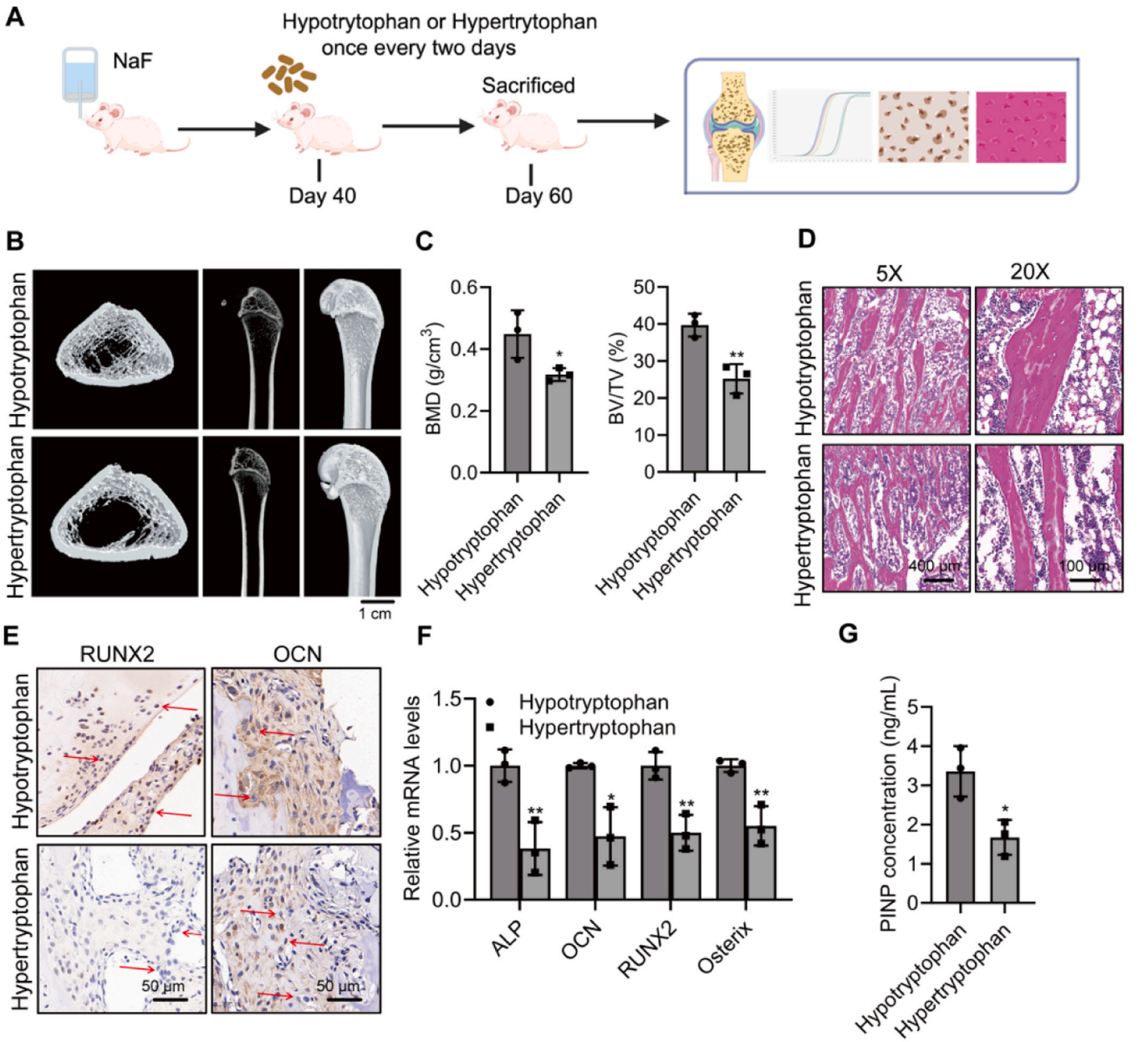

Fig. 6. High-tryptophan diet attenuates NaF-induced osteogenesis. (A) Experimental schedule of experiment. (B) Radiographs of femorals from hypotryptophan (n = 3) and hypertryptophan (n = 3) diet rats, demonstrating differences in bone density and structure. (C) Bone mineral density (BMD) and bone volume fraction (BV/TV) measurements from rats in (B). (D) HE-stained pathologic section of rats femoral. (E) Immunohistochemical staining for RUNX2 and OCN in femoral section, the arrow indicates osteoblasts. (F) Relative mRNA levels of bone-related genes (ALP, OCN, Runx2, and Osterix) in femorals of hypotryptophan (n = 3) and hypertryptophan (n = 3) diet rats normalized to GAPDH. (G) Serum levels of PINP in hypotryptophan (n = 3) and hypertryptophan (n = 3) diet rats, measured by ELISA. Data are presented as mean ± SD. ns, $p > 0.05$, *$p < 0.05$, **$p < 0.01$.

Emerging evidence underscores the role of the gut microbiota in bone remodeling via metabolite-mediated signaling (Ye et al., 2022; Lu et al., 2021), with gut dysbiosis implicated in metabolic bone diseases such as osteoporosis and osteoarthritis (Liu et al., 2021; Chen et al., 2023). Prior studies reveal that chronic fluoride exposure markedly reduces the abundance of Bifidobacterium, Faecalibacterium, and Bacteroides-genera essential for maintaining intestinal barrier integrity and regulating tryptophan metabolism (Mo et al., 2023; Zhong et al., 2022). Our research is consistent with previous observations showing that fluoride damages the intestinal barrier and alters gut microbiota composition in mice (Fu et al., 2022; Jin et al., 2022). We extend these findings, however, by demonstrating that fluoride exposure depletes bacterial taxa critical for tryptophan metabolism, thereby reducing the production of 3-IAA.Importantly, the loss of circulating 3-IAA, validated in both rodent models and SF patients, establishes 3-IAA as a functional link between gut dysbiosis and bone pathology.

The Wnt/β-Catenin signaling pathway is a key regulator of osteogenesis (Chu et al., 2020; Fei et al., 2019; Liu et al., 2020). Excessive activation of this pathway by fluoride accelerates bone matrix mineralization and disrupts the homeostasis of bone remodeling (Guo et al., 2022). While previous studies have linked Wnt pathway activation to fluoride-induced osteogenesis (Chu et al., 2020; Guo et al., 2022), none have identified a microbiota-derived metabolite as an upstream modulator. Our data mechanistically connect 3-IAA deficiency to osteoblast hyperactivation via the AHR/Wnt/β-Catenin signaling axis. AHR activation is known to suppress Wnt3a and β-Catenin expression (Han et al., 2021; Moreno-Marin et al., 2018), and consistent with this, AHR agonists have been shown to inhibit osteoblast differentiation (Ge et al.,

2018; Hsieh et al., 2024). Here we demonstrate that 3-IAA, an endogenous AHR agonist, binds to AHR to suppress Wnt3a/β-Catenin signaling in osteoblasts. This inhibitory effect is abolished by CH-223191 or by AHR knockdown, confirming that 3-IAA acts through AHR. Thus, the 3-IAA/AHR pathway emerges as a protective mechanism against pathological bone formation, one that is disrupted by fluoride toxicity. Unlike many other AHR antagonists, CH-223191 exhibits no detectable AHR agonist-like activity or estrogenic potency, indicating its specificity as an AHR antagonist (Kim et al., 2006). While we utilized CH-223191 to demonstrate the role of AHR in 3-IAA-mediated mitigation of NaF-induced osteogenesis, the potential for off-target effects must be considered. Like most pharmacological tools, CH-223191 may have off-targets unrelated to AHR that are not yet fully characterized (Rawls et al., 2020). These off-target effects could theoretically contribute modestly to the phenotypes observed in this study. Therefore, although our data support a central role for AHR, future studies should employ genetic approaches, to further confirm these findings and exclude the off-target effects.

As a microbial metabolite derived from intestinal tryptophan metabolism, 3-IAA has been identified as a potential biomarker in multiple disease contexts (Liabeuf et al., 2020; Tintelnot et al., 2023). While direct clinical evidence linking serum 3-IAA levels to SF severity remains limited, our study revealed a significant reduction of 3-IAA in the serum of SF patients, suggesting a potential association with impaired bone metabolism. Furthermore, clinical studies have shown that the tryptophan metabolic pathway within the gut microbiota of SF patients is markedly downregulated and correlates with abnormal bone mineral density (Chen et al., 2024a, 2024b). Building on these findings, we investigated whether intermittent high-tryptophan dietary supplementation could serve as an adjuvant strategy for SF management. Our results suggest that intermittent tryptophan supplementation may periodically activate AHR signaling, disrupt sustained Wnt hyperactivity, and rebalance bone formation and resorption. Clinically, this approach may offer a novel therapeutic strategy for managing skeletal fluorosis, particularly in endemic regions where fluoride exposure is unavoidable.

Several unresolved questions require further investigation. First, while certain gut bacteria are known to promote the production of 3-IAA (Li et al., 2025, 2024), the mechanism by which intestinal fluoride accumulation alters the microbiota remains unclear. Specifically, it is unknown whether fluoride selectively depletes 3-IAA-producing taxa or broadly disrupts tryptophan metabolism to reduce 3-IAA production. Second, although our data indicate that activation of the AHR significantly suppresses Wnt/β-Catenin signaling, the precise transcriptional targets or regulatory nodes through which this inhibition occurs have yet to be elucidated. Third, while dietary tryptophan supplementation in animal models effectively elevated circulating 3-IAA levels and mitigated fluoride-induced bone damage, its therapeutic efficacy in early-stage skeletal fluorosis in humans, as well as its long-term safety, requires validation through prospective clinical trials.

Existing literature indicates that AHR can suppress the Wnt/β-catenin signaling through multiple pathways: 1) In colon cancer cells, activated AHR exhibits E3 ubiquitin ligase activity and directly interacts with β-catenin, promoting its ubiquitination and subsequent proteasomal degradation, thereby reducing total β-catenin protein levels (Ohtake et al., 2007); 2) In various models, AHR activation downregulates the expression of R-spondin 2 (Rspo2) and R-spondin 3 (Rspo3). R-spondins are potent enhancers of Wnt signaling, and their reduction attenuates Wnt pathway activation (Branam et al., 2013); 3) AHR activation upregulates Wnt inhibitory factor 1 (WIF1), a secreted protein that binds to Wnt ligands and inhibits their activity (Filali et al., 2002; Wiese et al., 2006); 4) In prostate development models, AHR activation prevents the cytoplasmic accumulation and nuclear translocation of β-catenin in basal epithelial cells (Schneider et al., 2014). Future work will focus on the precise molecular mechanism by which AHR regulates Wnt/β-catenin signaling. specific mechanism by which AHR regulates Wnt/β-catenin signaling.

Although our animal model results confirm the therapeutic efficacy of the tryptophan diet against skeletal fluorosis, the translation of the protective effects of tryptophan diet into human clinical applications requires careful consideration. Human responses to dietary interventions are subject to high inter-individual variability (Chao et al., 2021; Martínez-Garay and Djouder, 2023). This heterogeneity may stem from several factors: 1) Gut microbiota composition: Substantial interpersonal differences exist in the capacity of gut microbiomes to metabolize tryptophan, directly influencing the production of endogenous AHR ligands (Beam et al., 2021); 2) Host genetic polymorphisms: Genetic variations in key genes of the AHR signaling pathway (such as AHR itself, CYP1A1, and others) may modulate individual responsiveness to dietary tryptophan supplementation; 3) Complex dietary backgrounds and lifestyle factors: Beyond strictly controlled laboratory environments, human dietary habits, metabolic statuses, and overall health conditions present considerable complexity that can significantly impact intervention outcomes (Martínez-Garay and Djouder, 2023). Therefore, before the intermittent tryptophan dietary strategy can be widely implemented in human populations, its effectiveness must be validated through prospective clinical studies involving larger, more heterogeneous cohorts with diverse genetic backgrounds and gut microbiota characteristics. Such investigations are essential to verify its efficacy and identify specific subpopulations most likely to benefit from this nutritional approach.

In summary, this study redefines the pathogenesis of SF by establishing a causal link between chronic fluoride exposure, gut microbiota dysbiosis, 3-IAA deficiency, and Wnt/β-Catenin-mediated aberrant bone mineralization. Furthermore, our investigation of an intermittent tryptophan-enriched dietary intervention demonstrates its potential to restore 3-IAA levels and modulate this pathological signaling cascade, offering a promising therapeutic strategy. This paradigm shift highlights the central role of the gut-bone axis and paves the way for microbiota-targeted approaches to alleviate the global burden of fluorosis.

CRediT authorship contribution statement

Wenji Wang: Writing – review & editing, Visualization, Supervision, Funding acquisition, Conceptualization. **Shengshan Xue:** Resources, Data curation, Conceptualization. **Wei Zhang:** Software, Project administration, Investigation, Conceptualization. **Xingchao Chen:** Data curation, Conceptualization. **Jiantong Wei:** Writing – review & editing, Writing – original draft, Supervision, Formal analysis, Data curation, Conceptualization. **yongping wang:** Writing – review & editing, Writing – original draft, Software, Methodology, Funding acquisition, Formal analysis, Data curation, Conceptualization. **Wenqiang Liang:** Methodology, Investigation, Formal analysis, Data curation. **Hao Chen:** Visualization, Validation, Supervision, Conceptualization. **Qingqing Qin:** Supervision, Formal analysis, Data curation. **Guohua Chen:** Software, Investigation, Conceptualization.

Funding

The author(s) disclosed receipt of the following financial support for the research, authorship, and/or publication of this article: This work was supported by grants from Innovative Research Team Project of Hexi University President's Fund (CXTD002), Young Scientists Research Project of Hexi University President's Fund (QN2024031), Gansu Provincial Health Industry Research Project (GSWSQN2024–21), Gansu Science and Technology Program Funding Project (25JRRG006), 2025 Gansu Provincial Science and Technology Program Self-financed Project (25JRRA841).

Declaration of Competing Interest

The authors declare that they have no known competing financial

interests or personal relationships that could have appeared to influence the work reported in this paper.

Appendix A. Supporting information

Supplementary data associated with this article can be found in the online version at doi:10.1016/j.ecoenv.2025.119520.

Data availability

The data that has been used is confidential.

References

Beam, A., Clinger, E., Hao, L., 2021. Effect of diet and dietary components on the composition of the gut microbiota. Nutrients 13 (8).

Bhawal, U.K., Lee, H.J., Arikawa, K., et al., 2015. Micromolar sodium fluoride mediates anti-osteoclastogenesis in Porphyromonas gingivalis-induced alveolar bone loss. Int J. Oral. Sci. 7 (4), 242–249.

Branam, A.M., Davis, N.M., Moore, R.W., et al., 2013. TCDD inhibition of canonical Wnt signaling disrupts prostatic bud formation in mouse urogenital sinus. Toxicol. Sci. 133 (1), 42–53.

Cao, J., Bao, Q., Hao, H., 2024. Indole-3-Carboxaldehyde alleviates LPS-induced intestinal inflammation by inhibiting ROS production and NLRP3 inflammasome activation. Antioxidants 13 (9).

Chao, A.M., Quigley, K.M., Wadden, T.A., 2021. Dietary interventions for obesity: clinical and mechanistic findings. J. Clin. Invest. 131 (1).

Chelakkot, C., Ghim, J., Ryu, S.H., 2018. Mechanisms regulating intestinal barrier integrity and its pathological implications. Exp. Mol. Med. 50 (8), 1–9.

Chen, C., Cao, Z., Lei, H., et al., 2024a. Microbial tryptophan metabolites ameliorate ovariectomy-induced bone loss by repairing intestinal AhR-mediated gut-bone signaling pathway. Adv. Sci. 11 (36), e2404545.

Chen, Y., Yang, C., Dai, Q., et al., 2023. Gold-nanosphere mitigates osteoporosis through regulating TMAO metabolism in a gut microbiota-dependent manner. J. Nanobiotechnol. 21 (1), 125.

Chen, Y., Yang, C., Deng, Z., et al., 2024b. Gut microbially produced tryptophan metabolite melatonin ameliorates osteoporosis via modulating SCFA and TMAO metabolism. J. Pineal Res. 76 (3), e12954.

Chu, Y., Gao, Y., Yang, Y., et al., 2020. beta-catenin mediates fluoride-induced aberrant osteoblasts activity and osteogenesis. Environ. Pollut. 265 (Pt A), 114734.

Cotti, S., Huysseune, A., Koppe, W., et al., 2020. More bone with less minerals? The effects of dietary phosphorus on the post-cranial skeleton in zebrafish. Int. J. Mol. Sci. 21 (15).

Ding, H., Yin, C., Yang, M., et al., 2023. Screening of differentially methylated genes in skeletal fluorosis of rats with different types and involvement of aberrant methylation of Cthrc1. Environ. Pollut. 332, 121931.

Fei, D., Zhang, Y., Wu, J., et al., 2019. Ca(v) 1.2 regulates osteogenesis of bone marrow-derived mesenchymal stem cells via canonical Wnt pathway in age-related osteoporosis. Aging Cell 18 (4), e12967.

Filali, M., Cheng, N., Abbott, D., et al., 2002. Wnt-3A/beta-catenin signaling induces transcription from the LEF-1 promoter. J. Biol. Chem. 277 (36), 33398–33410.

Fu, R., Niu, R., Li, R., et al., 2020. Fluoride-induced alteration in the diversity and composition of bacterial microbiota in mice colon. Biol. Trace Elem. Res. 196 (2), 537–544.

Fu, R., Niu, R., Zhao, F., et al., 2022. Exercise alleviated intestinal damage and microbial disturbances in mice exposed to fluoride. Chemosphere 288 (Pt 3), 132658.

Ge, L., Cui, Y., Cheng, K., et al., 2018. Isopsoralen enhanced osteogenesis by targeting AhR/ERalpha. Molecules 23 (10).

Guo, N., Yu, Y., Chu, Y., et al., 2022. miR-21-5p and canonical Wnt signaling pathway promote osteoblast function through a feed-forward loop induced by fluoride. Toxicology 466, 153079.

Han, H., Davidson, L.A., Hensel, M., et al., 2021. Loss of aryl hydrocarbon receptor promotes colon tumorigenesis in Apc(S580/+); Kras(G12D/+) Mice. Mol. Cancer Res. 19 (5), 771–783.

Han, L., Ma, C., Wu, Z., et al., 2024. AhR-STAT3-HO-1/COX-2 signalling pathway may restrict ferroptosis and improve hMSC accumulation and efficacy in mouse liver. Br. J. Pharm. 181 (1), 125–141.

Hsieh, C.W., Chang, L.H., Wang, Y.H., et al., 2024. Indoxyl sulfate inhibits osteogenesis in bone marrow mesenchymal stem cells through the AhR/Hes1 pathway. Int. J. Mol. Sci. 25 (16).

Jiang, N., Guo, F., Sun, B., et al., 2020. Different effects of fluoride exposure on the three major bone cell types. Biol. Trace Elem. Res. 193 (1), 226–233.

Jin, Y., Gao, X.Y., Zhao, J., et al., 2022. Estrogen deficiency aggravates fluoride-induced small intestinal mucosa damage and junctional complexes proteins expression disorder in rats. Ecotoxicol. Environ. Saf. 246, 114181.

Jing, W., Dong, S., Xu, Y., et al., 2025. Gut microbiota-derived tryptophan metabolites regulated by Wuji Wan to attenuate colitis through AhR signaling activation. Acta Pharm. Sin. B 15 (1), 205–223.

Kassem, M., Mosekilde, L., Eriksen, E.F., 1994. Effects of fluoride on human bone cells in vitro: differences in responsiveness between stromal osteoblast precursors and mature osteoblasts. Eur. J. Endocrinol. 130 (4), 381–386.

Khokher, M.A., Dandona, P., 1990. Fluoride stimulates [3H]thymidine incorporation and alkaline phosphatase production by human osteoblasts. Metabolism 39 (11), 1118–1121.

Kim, S.H., Henry, E.C., Kim, D.K., et al., 2006. Novel compound 2-methyl-2H-pyrazole-3-carboxylic acid (2-methyl-4-o-tolylazo-phenyl)-amide (CH-223191) prevents 2,3,7,8-TCDD-induced toxicity by antagonizing the aryl hydrocarbon receptor. Mol. Pharm. 69 (6), 1871–1878.

Li, H., Du, Y., Cheng, K., et al., 2024. Gut microbiota-derived indole-3-acetic acid suppresses high myopia progression by promoting type I collagen synthesis. Cell Discov. 10 (1), 89.

Li, W., Shangguan, W., Huang, W., et al., 2025. Gut Parabacteroides distasonis-derived Indole-3-acetic acid promotes phospholipid remodeling and enhances ferroptosis sensitivity via the AhR-FASN axis in bladder cancer. Adv. Sci., e04688

Liabeuf, S., Laville, S.M., Glorieux, G., et al., 2020. Difference in profiles of the gut-derived tryptophan metabolite indole acetic acid between transplanted and non-transplanted patients with chronic kidney disease. Int J. Mol. Sci. 21 (6).

Liu, J.H., Chen, C.Y., Liu, Z.Z., et al., 2021. Extracellular vesicles from child gut microbiota enter into bone to preserve bone mass and strength. Adv. Sci. 8 (9), 2004831.

Liu, Y., Fang, J., Zhang, Q., et al., 2020. Wnt10b-overexpressing umbilical cord mesenchymal stem cells promote critical size rat calvarial defect healing by enhanced osteogenesis and VEGF-mediated angiogenesis. J. Orthop. Transl. 23, 29–37.

Liu, J., Wang, H.W., Lin, L., et al., 2019. Intestinal barrier damage involved in intestinal microflora changes in fluoride-induced mice. Chemosphere 234, 409–418.

Lu, L., Chen, X., Liu, Y., et al., 2021. Gut microbiota and bone metabolism. FASEB J. 35 (7), e21740.

Martínez-Garay, C., Djouder, N., 2023. Dietary interventions and precision nutrition in cancer therapy. Trends Mol. Med. 29 (7), 489–511.

Mo, Z., Wang, J., Meng, X., et al., 2023. The dose-response effect of fluoride exposure on the gut microbiome and its functional pathways in rats. Metabolites 13 (11).

Moreno-Marin, N., Merino, J.M., Alvarez-Barrientos, A., et al., 2018. Aryl hydrocarbon receptor promotes liver polyploidization and inhibits PI3K, ERK, and Wnt/beta-Catenin signaling. iScience 4, 44–63.

Ohtake, F., Baba, A., Takada, I., et al., 2007. Dioxin receptor is a ligand-dependent E3 ubiquitin ligase. Nature 446 (7135), 562–566.

Qiao, L., Liu, X., He, Y., et al., 2021. Progress of signaling pathways, stress pathways and epigenetics in the pathogenesis of skeletal fluorosis. Int. J. Mol. Sci. 22 (21).

Rawls, K., Dougherty, B.V., Papin, J., 2020. Metabolic network reconstructions to predict drug targets and off-target effects. Methods Mol. Biol. 2088, 315–330.

Russell, W.R., Duncan, S.H., Scobbie, L., et al., 2013. Major phenylpropanoid-derived metabolites in the human gut can arise from microbial fermentation of protein. Mol. Nutr. Food Res 57 (3), 523–535.

Schneider, A.J., Moore, R.W., Branam, A.M., et al., 2014. In utero exposure to TCDD alters Wnt signaling during mouse prostate development: linking ventral prostate agenesis to downregulated β-catenin signaling. Toxicol. Sci. 141 (1), 176–187.

Sellami, M., Riahi, H., Maatallah, K., et al., 2020. Skeletal fluorosis: don't miss the diagnosis! Skelet. Radio. 49 (3), 345–357.

Taher, M.K., Momoli, F., Go, J., et al., 2024. Systematic review of epidemiological and toxicological evidence on health effects of fluoride in drinking water. Crit. Rev. Toxicol. 54 (1), 2–34.

Tintelnot, J., Xu, Y., Lesker, T.R., et al., 2023. Microbiota-derived 3-IAA influences chemotherapy efficacy in pancreatic cancer. Nature 615 (7950), 168–174.

Tsao, Y.T., Huang, Y.J., Wu, H.H., et al., 2017. Osteocalcin mediates biomineralization during osteogenic maturation in human mesenchymal stromal cells. Int J. Mol. Sci. 18 (1).

Veneri, F., Iamandii, I., Vinceti, M., et al., 2023b. Fluoride exposure and skeletal fluorosis: a systematic review and dose-response meta-analysis. Curr. Environ. Health Rep. 10 (4), 417–441.

Veneri, F., Vinceti, M., Generali, L., et al., 2023a. Fluoride exposure and cognitive neurodevelopment: systematic review and dose-response meta-analysis. Environ. Res 221, 115239.

Wei, W., Pang, S., Sun, D., 2019. The pathogenesis of endemic fluorosis: Research progress in the last 5 years. J. Cell Mol. Med 23 (4), 2333–2342.

Whitford, G.M., 1994. Intake and metabolism of fluoride. Adv. Dent. Res 8 (1), 5–14.

Wiese, C., Rolletschek, A., Kania, G., et al., 2006. Signals from embryonic fibroblasts induce adult intestinal epithelial cells to form nestin-positive cells with proliferation and multilineage differentiation capacity in vitro. Stem Cells 24 (9), 2085–2097.

Wu, S., Wang, Y., Iqbal, M., et al., 2022. Challenges of fluoride pollution in environment: Mechanisms and pathological significance of toxicity - A review. Environ. Pollut. 304, 119241.

Yamaguchi, M., 2012. Role of carotenoid beta-cryptoxanthin in bone homeostasis. J. Biomed. Sci. 19 (1), 36.

Ye, Y., Liu, Y., Cheng, K., et al., 2022. Effects of intestinal flora on irritable bowel syndrome and therapeutic significance of polysaccharides. Front Nutr. 9, 810453.

Zhong, N., Ma, Y., Meng, X., et al., 2022. Effect of fluoride in drinking water on fecal microbial community in rats. Biol. Trace Elem. Res. 200 (1), 238–246.